



HAL
open science

Kinetics of cubic to tetragonal transformation in Ni-V-X alloys.

Helena Zapolsky, Sebastien Ferry, Xavier Sauvage, Didier Blavette, Long-Qing Chen

► **To cite this version:**

Helena Zapolsky, Sebastien Ferry, Xavier Sauvage, Didier Blavette, Long-Qing Chen. Kinetics of cubic to tetragonal transformation in Ni-V-X alloys.. *Philosophical Magazine*, 2010, 90 (01-04), pp.337-355. 10.1080/14786430903179562 . hal-00556065

HAL Id: hal-00556065

<https://hal.science/hal-00556065>

Submitted on 15 Jan 2011

HAL is a multi-disciplinary open access archive for the deposit and dissemination of scientific research documents, whether they are published or not. The documents may come from teaching and research institutions in France or abroad, or from public or private research centers.

L'archive ouverte pluridisciplinaire **HAL**, est destinée au dépôt et à la diffusion de documents scientifiques de niveau recherche, publiés ou non, émanant des établissements d'enseignement et de recherche français ou étrangers, des laboratoires publics ou privés.



Kinetics of cubic to tetragonal transformation in Ni-V-X alloys.

Journal:	<i>Philosophical Magazine & Philosophical Magazine Letters</i>
Manuscript ID:	TPHM-08-Nov-0427.R2
Journal Selection:	Philosophical Magazine
Date Submitted by the Author:	02-Jul-2009
Complete List of Authors:	zapolsky, helena; University of Rouen, GPM, UMR 6634, Sciences Ferry, Sebastien; University of Rouen, GPM, UMR 6634, Sciences Sauvage, Xavier; University of Rouen, GPM, UMR 6634, Sciences Blavette, Didier; University of Rouen, GPM, UMR 6634, Sciences Chen, Long-Qing; Penn State University, Material Science and Engineering
Keywords:	microstructure, ordered intermetallics, simulation
Keywords (user supplied):	microstructure, ordered intermetallics, simulation



Kinetics of cubic to tetragonal transformation in Ni-V-X alloys.

H. Zapolsky^{a*}, S. Ferry^a, X. Sauvage^a, D. Blavette^a and L. Q. Chen^b

^aGPM, UMR 6634 CNRS - Université de Rouen, Avenue de l'Université - BP 12, 76801 Saint-Etienne-du-Rouvray France

^bDepartment of Material Science and Engineering, Penn State University, PA 16802, USA

Abstract

Computer simulations based on the Khachaturyan's Onsager diffusion equation have been performed to model the microstructure evolution during the cubic-to-tetragonal transformation in Ni-based alloys. A 2D model was employed. The fcc-DO₂₂ ordering has been studied as a model case of this type of transformations. A particular emphasis is on the formation mechanism of DO₂₂ monovariant structures. Computer simulations demonstrate that strain-induced interactions between coherent DO₂₂ precipitates lead to the formation of intermediate two-variant chessboard-like structures, which are found to be unstable and coalesce into subsequent single-variant maze structures. It is shown that the stability of the chessboard-like structures is very sensitive to lattice misfits. These simulation results are in good agreement with TEM observations.

Keywords: phase transformation kinetics, microstructure, precipitation, modelling

Corresponding author: tel. +33 232955042, fax:+33 232955052, e-mail: helena.zapolsky@univ-rouen.fr

1. Introduction

Characteristic microstructures, so-called tweed or twinned structures, have been observed frequently in various alloys which undergo cubic to tetragonal phase transformations, such as NiV, NiCoV, NiFeV, FePd and CoPt [1-5]. In these transformations, the new phase is tetragonal and can be formed in the three different orientations with respect to the cubic mother phase. One might expect that the three variants would be formed with equal probability. The formation of tetragonal phase precipitates in cubic matrix, however, inevitably introduces elastic strain and random arrangements of variants would result in a large increase in the elastic energy of the system. Consequently, it is well understood that formation of tweed or twinned structures is driven by the elastic strain energy reduction.

The precipitation of DO₂₂ tetragonal phase in Ni-based alloys is one of the examples of a cubic to tetragonal transition. In Ni-V-X systems, a low symmetry ordered phase (tetragonal Ni₃V phase with the DO₂₂ ordered structure) coexists with the high symmetry fcc parent Ni-V-X solid solution ("A1" phase). In such systems, the formation of the DO₂₂ tetragonal phase produces an anisotropic strain field due to the contraction and expansion of the tetragonal *a* and *c* axes against the cubic matrix. Lattice misfit strain along *a*- and *c*-axes of DO₂₂ phase, δ_{11} and δ_{33} , can be determined using following equations: $\delta_{11} = (a_{DO22} - a_{A1}) / a_{A1}$ and $\delta_{33} = (c_{DO22} / 2 - a_{A1}) / a_{A1}$, respectively. The tetragonal phase has three [100] orientation variants, The resulting microstructure exhibits a fine brick-like "multi-variant structure (MVS)", and the variants are found to be twin-related to each other across the {110} planes.

There have been a number of attempts to model microstructure evolution in systems with coexisting tetragonal and cubic phases. Recently, Y. Ni and A. G. Khachaturyan [6,7] studied using 3D modelling based on the phase field microelasticity (PFM) approach the formation of chessboard-like microstructure in cubic matrix with different initial concentrations. It was remarked that there are two thermodynamically distinct regions within the two-phase field of the phase diagram that described the equilibrium coexistence of the cubic and tetragonal phases. These regions are determined by the relative values of the free energies of the cubic and tetragonal phases as a function of their composition. It was shown that the transformation pathways to the chessboard-like microstructure are very different in these two thermodynamically distinct regions. Y. Le Bouar et al. [8-10] investigated the effect of elastic energy on the morphology of chessboard-like microstructures in Co-Pt and (CuAu)_{1-x}-Pt_x alloys. It was shown that the parent cubic phase (L₁₂ for Co-Pt and disordered fcc for (CuAu)_{1-x}-Pt_x) coexist with the three different orientation variants of the tetragonal L₁₀ ordered phase. In this case, the final microstructure is multi-variant and strongly depends on the misfits between the two coexisting phases. Wen et al predicted the similar chessboard-like and other complex multivariant precipitate structures during precipitation of an orthorhombic phase in a hexagonal Ti-Al-Nb alloy [11,12]. All these simulations show that strain energy is the dominant factor that determines the stability of CB microstructures.

In contrast to Co-Pt and other alloys, experiments revealed that long time aging of binary Ni-V alloys leads to monovariant microstructures [13-15]. It was shown that during coarsening, the major variants in initial MVS grow at the expense of minor variants and disordered A1 phase. To understand the influence of misfit on stability of MVS A. Suzuki and al. [13] have investigated the evolution of microstructure in ternary Ni-V-X (where X=Co,Fe and Nb) alloys. It was shown that the morphology of ordered precipitates as well as the habit plane between A1 and DO₂₂ structure can be changed by alloying the binary Ni-V system with Co,Fe and Nb atoms. It was concluded that the misfit strain ratio $d = \delta_{11} / \delta_{33}$ and the magnitude of δ_{11} are important in determining the habit plane and the shape of DO₂₂ particles.

As the magnitude of $|\delta_{11}|$ becomes smaller than 0.002, the shape of the DO₂₂ variant changes from plate to prism elongated along a-axis on the habit plane, resulting in chessboard microstructure. Therefore, the main objective of this work is to understand the underlying thermodynamic driving forces and kinetic mechanisms leading to the formation of monovariant microstructures in binary Ni-V systems as well as the stability of MVS during cubic to tetragonal transformation in ternary Ni-V-X alloys.

To predict the microstructure evolution and precipitation kinetics of binary Ni-V and ternary Ni-V-X alloys, 2D computer simulations are performed based on the Khachaturyan's microscopic diffusion equation. Simulation results were compared with our TEM observations for Ni-19.5%V binary system and with experimental data for ternary Ni-V-X (X=Co,Fe and Nb) extracted from literature [13].

2. Model

To investigate the morphological evolution in the Ni-V system, we employed a computer simulation model based on the Onsager-type microscopic diffusion equations first proposed by Khachaturyan [16]. For a binary alloy this equation can be written as:

$$\frac{dP(\mathbf{r}, t)}{dt} = \sum_{\mathbf{r}'} L(\mathbf{r} - \mathbf{r}') \left[\frac{\delta F}{\delta P(\mathbf{r}', t)} \right] \quad (1)$$

where $P(\mathbf{r}, t)$ is the probability of finding of a solute atom (Vanadium) at a given lattice site \mathbf{r} and at a given time t , $L(\mathbf{r} - \mathbf{r}')$ are the exchange probabilities between the atoms at lattice sites \mathbf{r} and \mathbf{r}' per unit time and F is the free energy of system. In the case of a cubic-to-tetragonal transformation the free energy of system contains two terms:

$$F = F_{\text{chem}} + E_{\text{elas}} \quad (2)$$

where the first term F_{chem} corresponds to the chemical energy and E_{elas} is the total elastic strain energy.

In this paper, the mean-field approach is used to calculate the chemical free energy of system. For the binary alloys the chemical energy is given by:

$$F_{\text{chem}} = \frac{1}{2} \sum_{\mathbf{r}, \mathbf{r}'} P(\mathbf{r})P(\mathbf{r}')V(\mathbf{r} - \mathbf{r}') + k_B T \sum_{\mathbf{r}} [P(\mathbf{r}) \ln P(\mathbf{r}) + (1 - P(\mathbf{r})) \ln(1 - P(\mathbf{r}))] \quad (3)$$

where $V(\mathbf{r} - \mathbf{r}')$ is exchange energy, T is the temperature and k_B the Boltzmann constant.

A thermodynamic model is developed using the static concentration wave (SCW) formalism applied to the DO₂₂ structure. This structure is generated by the wave vectors:

$$\mathbf{k}_1 = \frac{2\pi}{a_{A1}} (100) \text{ and } \mathbf{k}_2 = \frac{2\pi}{a_{A1}} (\frac{1}{2}10) \text{ where } \mathbf{k} = (k_x k_y k_z) \text{ and } k_x, k_y \text{ and } k_z \text{ are components of}$$

the vector \mathbf{k} along the x , y and z axes parallel to the [100], [010] and [001] directions in the reciprocal space of f.c.c. lattice and a_{A1} is the lattice parameter of the f.c.c. lattice. Using the SCW formalism, the probability distribution function $P(\mathbf{r}, t)$ for the DO₂₂ structure can be written as:

$$P(\mathbf{r}(x, y, z)) = c + \gamma_1 \eta_1 e^{2i\pi x} + \gamma_2 \eta_2 \cos\left(2\pi\left(\frac{x}{2} + y\right)\right) \quad (4)$$

where c is the nominal vanadium concentration of the alloy, η_1 and η_2 are the order parameters, they vary from 0 (disordered state) to 1 (fully ordered state). In the case of DO_{22} structure the coefficients of symmetry are $\gamma_1 = 1/4$ and $\gamma_2 = 1/2$. For the DO_{22} structure, there are three orientation and fourth translation variants. Substituting (4) into (3) gives the expression for the chemical free energy for a DO_{22} structure:

$$F_{\text{DO}_{22}} = \frac{1}{2} N c^2 V(\mathbf{k} = \mathbf{0}) + \frac{1}{2} N \left(\frac{\eta_1}{4}\right)^2 V(\mathbf{k}_1) + N \left(\frac{\eta_2}{4}\right)^2 V(\mathbf{k}_2) - T S_{\text{DO}_{22}} \quad (5)$$

where entropy S is:

$$S_{\text{DO}_{22}} = -N \cdot k_B \cdot \left\{ \begin{array}{l} \frac{1}{2} \left[\left(c - \frac{1}{4} \cdot \eta_1\right) \cdot \ln \left(c - \frac{1}{4} \cdot \eta_1\right) + \left(1 - c + \frac{1}{4} \cdot \eta_1\right) \cdot \ln \left(1 - c + \frac{1}{4} \cdot \eta_1\right) \right] + \\ \frac{1}{4} \left[\left(c + \frac{1}{4} \cdot \eta_1 + \frac{1}{2} \cdot \eta_2\right) \cdot \ln \left(c + \frac{1}{4} \cdot \eta_1 + \frac{1}{2} \cdot \eta_2\right) + \right. \\ \left. \left(1 - c - \frac{1}{4} \cdot \eta_1 - \frac{1}{2} \cdot \eta_2\right) \cdot \ln \left(1 - c - \frac{1}{4} \cdot \eta_1 - \frac{1}{2} \cdot \eta_2\right) + \right. \\ \left. \left(c + \frac{1}{4} \cdot \eta_1 - \frac{1}{2} \cdot \eta_2\right) \cdot \ln \left(c + \frac{1}{4} \cdot \eta_1 - \frac{1}{2} \cdot \eta_2\right) + \right. \\ \left. \left(1 - c - \frac{1}{4} \cdot \eta_1 + \frac{1}{2} \cdot \eta_2\right) \cdot \ln \left(1 - c - \frac{1}{4} \cdot \eta_1 + \frac{1}{2} \cdot \eta_2\right) \right] \end{array} \right\}$$

where N is the total number of sites. $V(\mathbf{k}) = \sum_{\mathbf{r}} V(\mathbf{r}) \cdot \exp(i \mathbf{k} \cdot \mathbf{r})$ is the Fourier transform of exchange energies. For a f.c.c. lattice and for the \mathbf{k} vectors which generate the DO_{22} ordered structure, we can write:

$$\begin{cases} V(\mathbf{k} = \mathbf{0}) = 12\omega_1 + 6\omega_2 + 24\omega_3 + 12\omega_4 \dots \\ V(\mathbf{k}_1) = -4\omega_1 + 6\omega_2 - 8\omega_3 + 12\omega_4 \dots \\ V(\mathbf{k}_2) = -4\omega_1 + 2\omega_2 + 8\omega_3 - 4\omega_4 \dots \end{cases} \quad (6)$$

where ω_1 , ω_2 , ω_3 and ω_4 are first-, second-, third- and fourth-nearest neighbour effective exchange interaction energies.

The elastic energy term was calculated using the elastic theory of multiphase coherent solids with homogeneous modulus approximation proposed in [16]. If the strain effect is predominantly caused by the long range order parameter heterogeneity, then the stress-free strain can be expanded with respect to the long range order fields. As the $\eta \rightarrow -\eta$ transition does not affect the macroscopic stress-free strain, the first non-vanishing term of the expansion is of second order in $\eta_p(\mathbf{r})$:

$$\varepsilon_{ij}^0(\mathbf{r}) = \sum_p \eta_p^2(\mathbf{r}) \varepsilon_{ij}^{00}(p)$$

where the tensor $\varepsilon_{ij}^{00}(p)$ describes the stress-free transformation strain from parent cubic phase to the pth orientation variant of the tetragonal phase. In this case and under stress free boundary conditions, the elastic strain energy is:

$$E_{\text{elas}} = \frac{1}{2} \sum_{p,q} \int \frac{d^3k}{(2\pi)^3} B_{pq}(\mathbf{n}) \left\{ \eta_p^2 \right\}_k \left\{ \eta_q^2 \right\}_k^* \quad (7)$$

where $\left\{ \eta_p^2(\mathbf{r}) \right\}_k$ is the Fourier transform of $\eta_p^2(\mathbf{r})$ and $\left\{ \eta_q^2(\mathbf{r}) \right\}_k$ is the Fourier transform of $\eta_q^2(\mathbf{r})$, $B_{pq}(\mathbf{n}) = c_{ijkl} \varepsilon_{ij}^{00}(p) \varepsilon_{kl}^{00}(q) - n_i \sigma_{ij}^0(p) \Omega_{jk}(\mathbf{n}) \sigma_{kl}^0(q) n_l$, $\mathbf{n} = \frac{\mathbf{k}}{k}$ is a unit vector and the function, c_{ijkl} is the elastic moduli tensor, $\sigma_{ij}^0(p) = c_{ijkl} \varepsilon_{kl}^{00}(p)$, and $\Omega_{ij}(\mathbf{n})$ is a Green function tensor which is inverse to the tensor $\Omega_{ij}^{-1}(n) = c_{ijkl} n_k n_l \cdot \left\{ \eta_p^2(\mathbf{r}) \right\}_k$ which is the Fourier transform of $\eta_p^2(\mathbf{r})$. The sign ' near integral has the meaning that $\mathbf{k} = \mathbf{0}$ is to be excluded from the integration. According to [8], for a cubic-tetragonal transformation with isotropic elasticity, the function $B_{pq}(\mathbf{n})$ can be written in 2D as:

$$\begin{cases} B_{xx}(\bar{\mathbf{n}}) = \frac{2\mu\delta_{33}^2}{1-\nu} \left([(1-d)n_1^2 - (1+\nu d)]^2 + (1-\nu^2)d^2 \right) \\ B_{yy}(\bar{\mathbf{n}}) = \frac{2\mu\delta_{33}^2}{1-\nu} \left([(1-d)n_2^2 - (1+\nu d)]^2 + (1-\nu^2)d^2 \right) \\ B_{xy}(\bar{\mathbf{n}}) = \frac{2\mu\delta_{33}^2}{1-\nu} \left((1-d)^2 n_1^2 n_2^2 + (1+\nu)d(1+d) \right) \end{cases} \quad (8)$$

where $d = \delta_{11}/\delta_{33}$, ν is the Poisson ratio and μ the shear modulus.

The local order parameters η_p in equation (7) can be defined as follows. As we remark previously, each orientation variant of the DO₂₂ unit cell is generated by two vectors. The x-variant is generated by $\mathbf{k}_{1x} = \frac{2\pi}{a_{A1}}(100)$ and $\mathbf{k}_{2x} = \frac{2\pi}{a_{A1}}(1/210)$ vectors, and y-variant by

$\mathbf{k}_{1y} = \frac{2\pi}{a_{A1}}(010)$ and $\mathbf{k}_{2y} = \frac{2\pi}{a_{A1}}(11/20)$ vectors. In our simulations, we distinguish the DO₂₂

phase using only two order parameters η_{1x} and η_{1y} . These two local order parameters are calculated using a small simulation box S_B (5x5 sites) around a given lattice site. In this case the order parameters can be defined as:

$$\begin{cases} \eta_{1x}(\mathbf{r}) = \exp(-i\mathbf{k}_{1x}\mathbf{r}) \cdot (\text{coeff}_{1x}(\mathbf{r}) \otimes P(\mathbf{r})) \\ \eta_{1y}(\mathbf{r}) = \exp(-i\mathbf{k}_{1y}\mathbf{r}) \cdot (\text{coeff}_{1y}(\mathbf{r}) \otimes P(\mathbf{r})) \end{cases} \quad (9)$$

where symbol \otimes represent the product of convolution and

$$\text{coeff}_p(\mathbf{r}) = \begin{cases} \frac{1}{N_B \gamma_p} \cdot \exp(i\mathbf{k}_p \cdot \mathbf{r}) & \text{if } \mathbf{r} \in S_B \\ 0 & \text{otherwise} \end{cases} \quad p=1x \text{ or } 1y$$

Here N_B is the number of sites in S_B and γ_p is the symmetry coefficients in eq. (4). $\gamma_p=1/4$ for η_{1x} and η_{1y} . In the case of the order parameters associated to wave vectors \mathbf{k}_{1x} and \mathbf{k}_{1y} , the coefficients coeff_{1x} and coeff_{1y} can be represented in the matrix form:

$$\text{coeff}_{1x} = \frac{1}{4} \begin{pmatrix} 1/4 & -1/2 & 1/2 & -1/2 & 1/4 \\ 1/2 & -1 & 1 & -1 & 1/2 \\ 1/2 & -1 & 1 & -1 & 1/2 \\ 1/2 & -1 & 1 & -1 & 1/2 \\ 1/4 & -1/2 & 1/2 & -1/2 & 1/4 \end{pmatrix} \quad \text{and} \quad \text{coeff}_{1y} = \frac{1}{4} \begin{pmatrix} 1/4 & 1/2 & 1/2 & 1/2 & 1/4 \\ -1/2 & -1 & -1 & -1 & -1/2 \\ 1/2 & 1 & 1 & 1 & 1/2 \\ -1/2 & -1 & -1 & -1 & -1/2 \\ 1/4 & 1/2 & 1/2 & 1/2 & 1/4 \end{pmatrix}$$

where each element is calculated at site $\mathbf{r}=\mathbf{a}(m,n)$ where m and n are integer values and vary from -2 to 2 and $\mathbf{a}=\mathbf{a}_{A1}/2$ is the lattice parameter of disordered f.c.c. phase in 2D.

Due to the periodic boundary conditions applied to the simulations box, the equation (7) can be rewritten in the discrete form as follows:

$$E_{\text{elas}} = \frac{v_0}{2N} \sum_{p,q} \sum_{\mathbf{k} \in B_1} B_{pq}(\mathbf{n}) \left\{ \eta_{1p}^2(\mathbf{r}, t) \right\}_{\mathbf{k}} \left\{ \eta_{1q}^2(\mathbf{r}, t) \right\}_{\mathbf{k}}^* \quad (10)$$

where v_0 is the fcc unit cell volume, N is the number of sites in the simulation box, and the summation is carried over the first Brillouin zone B_1 . With definitions (9), equation (10) gives explicitly the elastic energy for a given probability distribution function $P(\mathbf{r}, t)$. In this form the elastic energy can be directly incorporated in the Onsager equation.

3. Experimental results

The investigated alloy had a nominal composition of 19.5 at.% V (Ni balance). A $\langle 001 \rangle$ oriented single crystal rod was cast by the withdrawal process at ONERA (Office National d'Etudes et de Recherches Aéropatiales). This alloy was then annealed at 1300°C for 3h and quenched in iced water. Finally, aging treatments were performed at 800°C for 15 min, 1h, 3h and 10h. Samples were cut with a drilling machine from the single crystal and mechanically thinned down to 100 μm . The electron transparency of the specimens was achieved with a twin-jet electropolisher, using 2% perchloric acid in 2-butoxyethanol solution at 20°C with a voltage of 30V. Observations were made with a JEOL 2000FX microscope operating at 200kV.

Figure 1

Figure 2

1
2
3
4
5
6
7
8
9
10
11
12
13
14
15
16
17
18
19
20
21
22
23
24
25
26
27
28
29
30
31
32
33
34
35
36
37
38
39
40
41
42
43
44
45
46
47
48
49
50
51
52
53
54
55
56
57
58
59
60

Selected area electron diffraction (SAED) patterns were recorded along the [001] fcc axis in samples aged 15 min, 1h, 3h and 10h at 800°C. In the early stage of the precipitation and coarsening, the three variants of the DO₂₂ phase are clearly seen (Figure 1a). At intermediate time, only two variants remain in the alloy (Figure 1b and c). Finally, for longer ageing treatment, only one variant of the ordered DO₂₂ phase is present (Figure 1d).

In the early stage of ageing (15 min) at 800°C, DO₂₂ ordered precipitates are smaller than 10 nm, which makes them very difficult to image. Figure 2(a) shows a dark field image of the microstructure after 3 hour of ageing at 800°C. This image was obtained from superlattice reflections of the two variants of the DO₂₂ phase ([100] and [010]) and thus highlights all DO₂₂ precipitates. These precipitates are parallelogram-shaped and this image shows a typical “chessboard” microstructure with a wide range of precipitate sizes. It is interesting to note that the microstructure is periodically aligned along $\langle 201 \rangle_{\text{DO}_{22}} // \langle 110 \rangle_{\text{Al}}$. Moreover, if only one superlattice reflection is selected to image only one variant, laths of precipitates are seen (figure 2b), indicating that DO₂₂ variants are not randomly distributed. Precipitates of one of the variants are clearly aligned along $\langle 110 \rangle$ directions and depletion bands aligned along the same direction are observed.

After 10h of aging at 800°C (Figure 2c), the “chessboard” microstructure has vanished. Only one variant of the DO₂₂ phase remains, and precipitates are quadrangular-prism shaped. Moreover, at this step of the coarsening process, the orientation of precipitates is slightly tilted so that the angle between the invariant plane and $\langle 110 \rangle_{\text{Al}}$ is 8° ($\pm 2^\circ$).

4. Simulations.

4.1 Selective growth of DO₂₂ variants in Ni-V alloys.

The kinetic equation (1) was numerically solved in reciprocal space using the explicit forward Euler technique. Two-dimensional simulation was performed with a 768x768 sites box, corresponding to 135nm x 135 nm. Periodic boundary conditions were applied. Nominal Vanadium composition was fixed at 20%_{at}. The system was started from a homogeneous disordered state with 1500 randomly distributed small DO₂₂ precipitates (x and y-variants each with 4 translation variants). According to the experimental results presented in [17], we have used the following set of elastic parameters : $T=1000^\circ\text{C}$, $\mu=367 \text{ meV}/\text{\AA}^3$, $\nu=1/3$, $\delta_{11}=-0.0053$ and $\delta_{33}=0.0106$. The exchange energies were fitted to the experimental phase diagram [18]. The free energies of the DO₂₂ ordered phase as a function of composition at a given temperature are obtained by minimisation of chemical free energy (5) with respect to the order parameters. Finally, the equilibrium compositions of ordered and disordered phases were determined numerically by the common tangent construction. A reasonably good fit was obtained using the following chemical interaction parameters with a third-neighbour interaction model: $\omega_1= 93.33 \text{ meV}$; $\omega_2= -27.92 \text{ meV}$; $\omega_3= -25.10 \text{ meV}$. The free energy curves for the ordered and disordered phases as a function of composition at $T = 800^\circ\text{C}$ are shown in Fig. 3. The simulated Ni-20%V alloy are situated in the region of phase diagram where the free energy of the tetragonal phase is lower than that of the cubic disordered phase at the same composition. As was noted in [6], in this region the transformation can start as a congruent (diffusionless) crystal lattice rearrangement. However, from our previous 3D atom probe analyses [19] the composition heterogeneities were observed at the very early stages of precipitation. Therefore, we will consider only the diffusion path for the cubic to tetragonal transformation in the Ni-V systems.

Figure 3

We assumed that diffusion jumps take place only between nearest-neighbour lattice sites, so that $L(\mathbf{r}-\mathbf{r}')$ is equal to L_1 if sites \mathbf{r} and \mathbf{r}' are first-neighbour and 0 for further neighbour order. To initiate the simulation, precipitates were artificially introduced in the simulated box. This implies that information on the early stages of nucleation, like the incubation time, is not available from such simulations. The simulation time is measured in reduced time ($t^*=L_1t$) where L_1 can be related to the diffusion coefficient. Our emphasis is on the influence of elastic interactions on the coarsening kinetics, and in particular on the relative stability of orientation variants of Ni_3V precipitates.

The microstructural evolution in a Ni-20%_{at}V alloy is presented in Fig. 4. The x- and y-variants are represented in white and grey respectively. Disordered fcc matrix is in black. The initial stage microstructure (4a: $t^*=4$) consists of rectangular ordered domains with characteristic alignment along the $\langle 110 \rangle$ directions. Both orientational variants are present but bands of monovariants aligned along the $\langle 110 \rangle$ direction start to be formed. At $t^*=30$ (Fig. 4b), the microstructure is composed of alternating monovariant bands aligned along the $\langle 110 \rangle$ direction. At this stage we also observe the independent coarsening of ordered domains in each monovariant bands. We would like to remark that some of these domains are separated by antiphase boundaries. At $t^*=120$ (Fig. 4c), local coarsening is finished, and DO_{22} precipitates form chessboard-like structure. The next stage of kinetics involves a non-local coarsening phenomenon. At this stage, the entire rows of y-variant precipitates disappear, and the structure becomes mono-variant (Fig. 4d).

Figure 4

The evolution of volume fraction of each variant is represented in fig.5. This figure demonstrates that y-variant starts to disappear from $t^*>200$, when the local coarsening in each variant road is finished.

Figure 5

These simulation results reproduce quite well the experimentally observed microstructure evolution in Ni-V alloy aging from 1 h to 10 h at 800°C (see Figure 2).

4.2 Influence of misfit ratio on chessboard-like microstructure.

Figure 6 gives a comparison of simulated and experimental chessboard-like structures. Microstructures including the size of precipitates (~ 50 nm) from the experiments and simulations are similar. However, there is a disagreement in elastically soft directions. In contrast to simulation (fig. 6a), TEM image (fig. 6b) reveals a slight misorientation of facets of precipitates. The angle of facets with respect to $\langle 110 \rangle_{A1}$ is $8^\circ (\pm 2^\circ)$. As has been shown by Le Bouar et al. in [8], there is a relation between this angle and the misfit ration d :

Figure 6

$$\sin^2 \alpha_x = (1 + \nu) \frac{-d}{1-d} \quad (11)$$

where α_x is the soft direction angles of x-variant, with respect to the [100] axis and ν the Poisson coefficient. The Poisson coefficient was taken equal to 1/3.

Figure 7

Figure 7 shows the dependence of x-variant soft direction with respect to the misfit ratio d (equation (11)). On this figure we indicated (grey square) the misfit measured by A. Suzuki et al [13]. This misfit corresponds to $\alpha_x \approx 42^\circ$. In our TEM images we find $\alpha_x \approx 37^\circ$ (black square on Figure 7). The observed discrepancy between two measurements can be explained by two reasons. Firstly, there is normal experimental incertitude in measurements of misfit and secondly, as was observed in [13] the angles α_x can vary during coarsening.

In order to better reproduce elastically soft direction in our simulations, a small correction of misfit was applied: we chose $d = \delta_{11}/\delta_{33} = -0.35$ and $\delta_{11} - \delta_{33}$ was arbitrarily set to a constant. New misfits used in simulation were $\delta_{11} = -0.0041$ and $\delta_{33} = 0.0118$ (instead of $\delta_{11} = -0.0053$ and $\delta_{33} = 0.0106$ previously). Figure 8 shows the new microstructure simulated with $d = -0.35$. Orientations of facets of precipitates are now quite well reproduced and correspond to the chessboard-like microstructure observed experimentally (see Figure 6b).

Figure 8

Microstructure evolution at early stages was found to be quite similar for both values of d . After forming monovariant bands, the precipitates coarsen independently in each band and create the chessboard-like structure. Once formed, the two-variant chessboard-like structure again is unstable. However, the disappearance of the last variant is much slower than the previous simulation. Our simulation has never reached the entire disappearance because of the longer time needed. By comparing the disappearance rates of the two simulations at the same variant volume fraction $\Phi_x = 0.39$ (see figure 4d), we observed that chessboard-like structure in the second simulation evolves slower than first simulation.

By comparing both simulations ($d = -0.5$ with $\delta_{11} = -0.0053$ and $\delta_{33} = 0.0106$ and $d = -0.35$ with $\delta_{11} = -0.0041$ and $\delta_{33} = 0.0118$), we conclude that the final microstructure strongly depends on the misfit ratio d . The decrease in misfit ratio significantly reduces the rate of disappearance of one of the DO_{22} variants. This strong dependence of the stability of the two-variant chessboard-like structure on misfit has been showed experimentally and by phase field modelling [20]. Suzuki et al. [13,14] have studied the alloying effect on the stability of multi-variant structures in Ni_3V at elevated temperatures. They examined microstructures in several alloys (Ni-V or Ni-V-M where M is an alloying element such as Iron, Niobium and Cobalt). It was shown that the stability of the chessboard-like structure increases with the decrease in the magnitude of misfit δ_{11} . The same tendency was found in our simulations. The chessboard-like structure is more stable for δ_{11} equal to 0.0041 than 0.0053.

To understand better the influence of the misfit on final microstructure we simulated the kinetic evolution in Ni-V system with the value of misfit obtained for Ni-V-Nb and Ni-V-Co systems [13]. In these ternary alloys the Nb and Co atoms occupy the same site in the crystal lattice as V and participate in the formation of DO₂₂ structure. It was shown in [13] that Nb atoms drastically decrease the misfit between DO₂₂ phase and the f.c.c. matrix. The misfit ratio d in this case is approximately 0.

Figure 9

Figure 9 shows the microstructure at $t^*=150$. This simulation reveals that for $d=0$ the volume fraction of each orientation variant remains constant and x- and y-variant coexist during all simulation time. The topology of microstructure is chessboard-like, but the ordered precipitates aligned along the $\langle 100 \rangle$ and $\langle 010 \rangle$ directions. This microstructure reproduces quite well the dark field images for Ni-15%V-5%Nb obtained in [13].

4.3 Elastic terms

The elastic energy of the two-variant system can be written as a sum of three terms:

$$E_{\text{elas}} = E_{XX} + E_{YY} + E_{XY} \quad (12)$$

where

$$\begin{cases} E_{XX} = \frac{1}{2} \int \frac{d^3 \vec{k}}{(2\pi)^3} B_{xx}(\vec{n}) |\eta_x(\vec{k})|^2 \\ E_{YY} = \frac{1}{2} \int \frac{d^3 \vec{k}}{(2\pi)^3} B_{yy}(\vec{n}) |\eta_y(\vec{k})|^2 \\ E_{XY} = \frac{1}{2} \int \frac{d^3 \vec{k}}{(2\pi)^3} B_{xy}(\vec{n}) [\eta_x(\vec{k}) \eta_y^*(\vec{k}) + \eta_y(\vec{k}) \eta_x^*(\vec{k})] \end{cases}$$

The first and second terms E_{XX} (E_{YY}) in elastic energy take into account the elastic interactions between the same variant domains. The third term E_{XY} reproduces elastic interaction energy between the two different variants. The misfits used in simulation are $\delta_{11} = -0.0041$ and $\delta_{33} = 0.0118$.

To understand the influence of each elastic term on the microstructural evolution and on the shape of precipitates, two simulations have been realised. The first simulation takes into account the $E_{XX}+E_{YY}$ terms only, E_{XY} being put zero.

Figure 10

Figure 11

As shown in Figure 10, if only elastic interactions between the same variants are taken into account, the chessboard-like structure is not observed, and one of the variants is observed vanish rapidly (less than 10 unities of reduced time). This mono-variant structure is similar to the maze structure observed in TEM images (Figure 2c). Figure 11 shows the

1
2
3 evolution of E_{XX} , E_{YY} and $E_{XX}+E_{YY}$ during the simulation. The minimization of elastic energy
4 due to the variant disappearance is clearly visible. The total elastic energy ($E_{XX}+E_{YY}$)
5 decreases by half after one of the variant disappeared. It clearly shows that E_{XX} and E_{YY}
6 elastic terms are responsible for the formation of mono-variant microstructure.
7

8 In the second simulation, only E_{XY} terms were taken into account ($E_{XX}=E_{YY}=0$).
9 Figure 12 shows the microstructural evolution of two-variant structures at different reduced
10 times. Figure 13(a-b) represents the evolution of the volume fractions of each variant and
11 variation with reduced time of E_{XY} , respectively. In this case, the chessboard-like structure is
12 clearly generated. Each precipitate of one of variants tends to be surrounded by 4 precipitates
13 of the other variant along $\langle 100 \rangle$ directions. The shape of precipitates is nearly spherical. This
14 indicates that E_{XY} elastic term is responsible only for alignments of precipitates. As we can
15 see in Figure 13(a), the volume fractions of each variant are equal and stay constant and there
16 is no competitive growth between two variants. As we can see on Figure 13(b), the E_{XY} elastic
17 contribution is negative due to the opposite sign between δ_{11} and δ_{33} values. So if one variant
18 will disappear then the E_{XY} term tends to zero. We can conclude that the E_{XY} term makes the
19 two-variant structures stable.
20
21
22

23 Figure 12

24 Figure 13

25
26
27
28 These two simulations in this section demonstrate that the E_{XY} term is mainly
29 responsible for the creation and the stability of the two variant chessboard-like structure while
30 the $E_{XX}+E_{YY}$ elastic terms induce the instability of the two variant structure and push the
31 system to form mono-variant microstructure. The real microstructure is formed by
32 minimisation of total elastic energy which is a result of a competition between E_{xx} (E_{yy}) and
33 E_{xy} terms as well as chemical free energy.
34

35 In order to better understand the influence of E_{XX} and E_{YY} terms on the shape of
36 precipitates we calculated the value of B_{XX} as function of angle θ which defines the angle
37 between the unit vector \vec{n} normal to matrix/precipitate interface and $\langle 100 \rangle$ direction of cubic
38 lattice. Figure 14a represents the typical shape of x-variant precipitate of the chessboard-like
39 structure. On this figure we indicated the vectors normal to the habit planes. Figure 14b
40 shows that the function B_{XX} reaches minima at $\theta=35^\circ$ and in the perpendicular direction. This
41 is a reason why a precipitate will try to have a maximum interface in this direction. The
42 directions $\langle 100 \rangle$ and $\langle 010 \rangle$ correspond to the maximum value of B_{XX} . Therefore the
43 interfaces along these directions are energetically unfavourable. In this case the minimisation
44 of elastic energy leads to decreasing of the surface of these interfaces and forms the corners.
45 This configuration will increase the total interface of ordered particle and consequently the
46 chemical interface energy. The minimisation of chemical interface energy will try to smooth
47 the corners of precipitate. The competition between these two phenomena will give the
48 equilibrium shape of precipitate.
49
50
51
52

53 Figure 14

54
55 The function B_{XX} in fig.14b was evaluated with input parameters of Ni-V system and with the
56 misfit ration $d=-0.35$. It should be noted that the height of two maxima is different for two
57 perpendicular directions. To check the influence of the values of these maxima on the shape
58 of corners of precipitates we performed the simulation where from $t^*=400$ the shape of B_{XX}
59 curve was artificially modified as shown in fig.15.
60

Figure 15

Fig.16a presents the microstructure at $t^*=400$. We can remark that two adjacent corners of ordered particles have different curvature. Figure 16b shows the microstructure at $t^*=500$, after 100 step of simulation with modified function B_{xx} . We can note that the curvature of all fourth corners of precipitates is the same.

Figure 16

These results show that we can predict the behaviour of the function $B(\vec{n})$ from TEM observations. TEM images can give not only the information about elastically soft directions but also the values of maxima of the $B(\vec{n})$.

5. Summary and conclusions

TEM investigations of the early stages of aging indicate that the spacing between precipitates is relatively large so that the multivariant structure is observed. Our simulations reveal that at this stage a two variant structure is formed and these two DO_{22} variants align along the $\langle 110 \rangle$ directions. During the later stages of coarsening, experimental data and simulations show that major variant grows at the expense of the minor variant and a monovariant structure is eventually observed. The habit plane makes an angle of 37° with respect to the $[100]_{DO_{22}}$ (a-axis). It has been shown that the misfit ratio $d=\delta_{11}/\delta_{33}$ has a significant effect on the stability of two-variant chessboard-like microstructures. Simulations results reproduce quite well TEM observed microstructures.

Acknowledgements- The authors gratefully acknowledge Dr. P. Caron (ONERA, France) for the Ni-V single crystal growth. The simulations were carried out in the CRIHAN centre under project 1999006.

References

- [1] B. Zhang, M. Lelovic, and W.A. Soffa, *Scr. Metall. Mater.* 25 (1991), p.1577.
- [2] A. Suzuki, and M.J. Takeyama, *Mater. Res.* 21 (2001), p.21.
- [3] G.M. Guschin, and F.N. Berseneva, *Phys. Met. Metallogr.* 63(1987), p.83.
- [4] R. Oshima, M. Yamashita, K. Matsumoto, and K. Higara, in *Proceeding of Solid-Solid Phase Transformations*, ed. By W.C. Johnson, J.M. Howe, D.E. Laughlin, and W.A. Soffa (The Minerals, Metals & Material Society, PA, 1994), p.407.
- [5] M.S. Muto, R. Oshima, and F.E. Fujita, *Acta Metall. Mater.* 38(1990), p.685.
- [6] Y. Ni, and A. G. Khachaturyan, *Acta Mater.* 56 (2008), p.4498.
- [7] Y. Ni, Y.M. Jin, and A. G. Khachaturyan, *Acta Mater* 55 (2007), p.4903.
- [8] Y. Le Bouar and A.G. Khachaturyan *Acta Mater* 48 (2000), p.1707.
- [9] Y. Le Bouar and A. Loiseau *Acta Mater* 49 (2001), p.2679.
- [10] Y. Le Bouar, A. Loiseau and A.G. Khachaturyan, *Acta Mater* 46 (1998), p.2777.
- [11] Y. H. Wen, Y. Wang, and L. Q. Chen, *Acta Mater* 49 (2001), p. 2341.
- [12] Y. H. Wen, Y. Wang, L. A. Bendersky, and L. Q. Chen, *Acta Mater* 48 (2000), p. 4125.
- [13] A. Suzuki, H. Kojimi, T. Matsuo, and M. Takeyama *Intermetallics* 12 (2004), p.969.
- [14] A. Suzuki, M. Takeyama, and T. Matsuo *Mat. Res. Symp. Proc* 753 (2003), p.363.
- [15] J.B. Singh, M. Sundararaman, P. Mukhopadhyay, and N. Prabhu, *Intermetallics* 11 (2003), p.83.
- [16] A. G. Khachaturyan *Theory of Structural Transformations in Solids*, Wiley, New York, 1983.
- [17] D.K. Na D, J.B. Cohen, and P.W. Voorhees, *Mater Sci Eng A* 272 (1999), p.10.
- [18] M.F. Singelton, J.L. Murray, P. Nash *Binary Alloy Phase Diagrams*, eds Massalski TB, Muray JL, Bennet LH, Baker H, Metals Park, Ohio: American Society for Metals, 1986.
- [19] H. Zapolsky, C. Pareige and D. Blavette, and L.Q. Chen *CALPHAD* 21 (2001), p.125.
- [20] T. Koyama, and H. Onodera, *Materials Science Forum*, 561-565 (2007), p.2287.

Figure captions

- Figure 1 : SAED patterns performed along [001] f.c.c. axis in the Ni-19.5at.%V alloy aged 15 min (a), 1 h (b), 3 h (c) and 10 h (d) at 800°C . Superlattice reflections corresponding to the 3 variants x, y and z of the DO₂₂ phase are labelled I, II and III respectively.
- Figure 2 : (a) Dark field image showing the two DO₂₂ variants in the alloy aged 3 h at 800°C. (b) dark field image showing only one DO₂₂ variant (x) in the same alloy, (c) Dark field image showing the only variant remaining after 10 h aging at 800°C.
- Figure 3 : Free energy of disordered f.c.c. phase (in grey) and ordered DO₂₂ phase (in black) versus composition for Ni-V system for T=800°C.
- Figure 4 : Morphological evolution of DO₂₂ precipitates from 2D simulations in a Ni-20%_{at}V at different reduced time : (a) t*=4 ; (b) t*=30 ; (c) t*=120 and (d) t*=750. x- and y-variant are represented in white and grey, respectively. Disordered fcc matrix is in black. Computational domain size is 135nmx135 nm. Periodic boundary conditions have been applied to construct these images.
- Figure 5: Evolution of volume fraction of x-(in black) and y-(in grey) orientation variants of DO₂₂ structure.
- Figure 6: Comparison of precipitate morphologies obtained by simulations (a) and experiments (b): a)simulation at t*=150 (b) dark field image showing the two DO₂₂ variants in Ni-19.5%_{at}V aged 3 h at 800°C. x- and y-variant are represented in white and grey respectively. Disordered fcc matrix is in black.
- Figure 7 : Evolution of elastically soft direction α_x for x-variant with respect to the misfit ratio d given by equation (11). Poisson coefficient is fixed at 1/3. The grey square corresponds to the measured misfits by [13]. The black square corresponds to the measured soft direction ($\alpha_x=37^\circ$) from our TEM images.
- Figure 8: Simulated microstructure at t*=750. In this simulation the misfit parameters are $\delta_{11}=-0.0041$ and $\delta_{33}=0.0118$ and $d=\delta_{11}/\delta_{33}=-0.35$. x- and y-variant are represented in white and grey respectively. Disordered fcc matrix is in black. The image represents 1.5 the length of simulation box. To obtain this image the periodic boundary conditions have been applied.
- Figure 9: Simulated microstructure at t*=150. In this simulation the misfit ratio d=0. x- and y-variant are represented in white and grey respectively. Disordered fcc matrix is in black. The image represents 1.5 the length of simulation box. To obtain this image the periodic boundary conditions have been applied.
- Figure 10: Microstructure evolution with $E_{XY}=0$. ($\delta_{11}=-0.0041$ and $\delta_{33}=0.0118$) at different reduced time (a)t*=2.5 (b) t*=5, (c) t*=10 and (d) t*=20.
- Figure 11: Evolution of the elastic energy E_{XX} , E_{YY} and E_{XY} as function of reduced time in Ni-20%V aged at 800°C ($\delta_{11}=-0.0041$ and $\delta_{33}=0.0118$).
- Figure 12: Microstructure with $E_{XX}=E_{YY}=0$. ($\delta_{11}=-0.0041$ and $\delta_{33}=0.0118$) (a), (b) and (c): correspond to t*=2.5, 10 and 20 respectively.

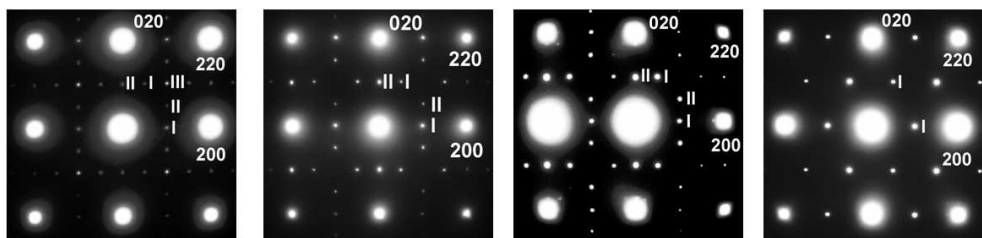
1
2
3 Figure 13: Simulation with $E_{XX}=E_{YY}=0$. ($\delta_{11} = -0.0041$ and $\delta_{33} = 0.0118$) (a): variation of
4 volume fractions with time (b): time evolution of the E_{XY} elastic term.
5
6

7 Figure 14: a) Shape of x-variant precipitate. The arrows 1,2 and 3,4 indicate the directions
8 where B_{xx} has minima and maxima, respectively, b) function B_{xx} versus angle θ .
9

10 Figure 15: Function B_{xx} versus angle θ . Initial (in black) and modified (in grey).
11

12 Figure 16. : Microstructure with (a) B_{xx} of Ni-V system, (b) B_{xx} modified. White lines
13 indicate the orientations of the facets of precipitates.
14
15
16
17
18
19
20
21
22
23
24
25
26
27
28
29
30
31
32
33
34
35
36
37
38
39
40
41
42
43
44
45
46
47
48
49
50
51
52
53
54
55
56
57
58
59
60

For Peer Review Only



(a): 15 min

(b): 1 h

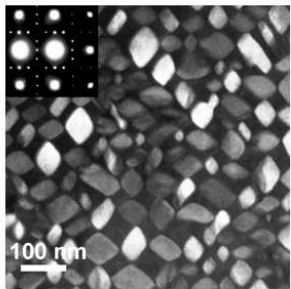
(c): 3h

(d): 10 h

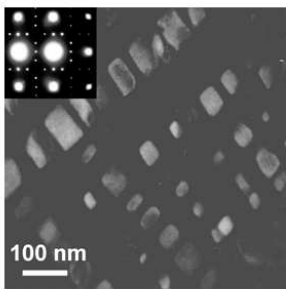
313x105mm (96 x 96 DPI)

Peer Review Only

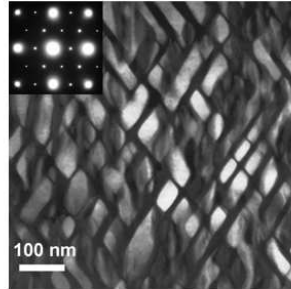
1
2
3
4
5
6
7
8
9
10
11
12
13
14
15
16
17
18
19
20
21
22
23
24
25
26
27
28
29
30
31
32
33
34
35
36
37
38
39
40
41
42
43
44
45
46
47
48
49
50
51
52
53
54
55
56
57
58
59
60



(a) variants x and y



(b) variant x

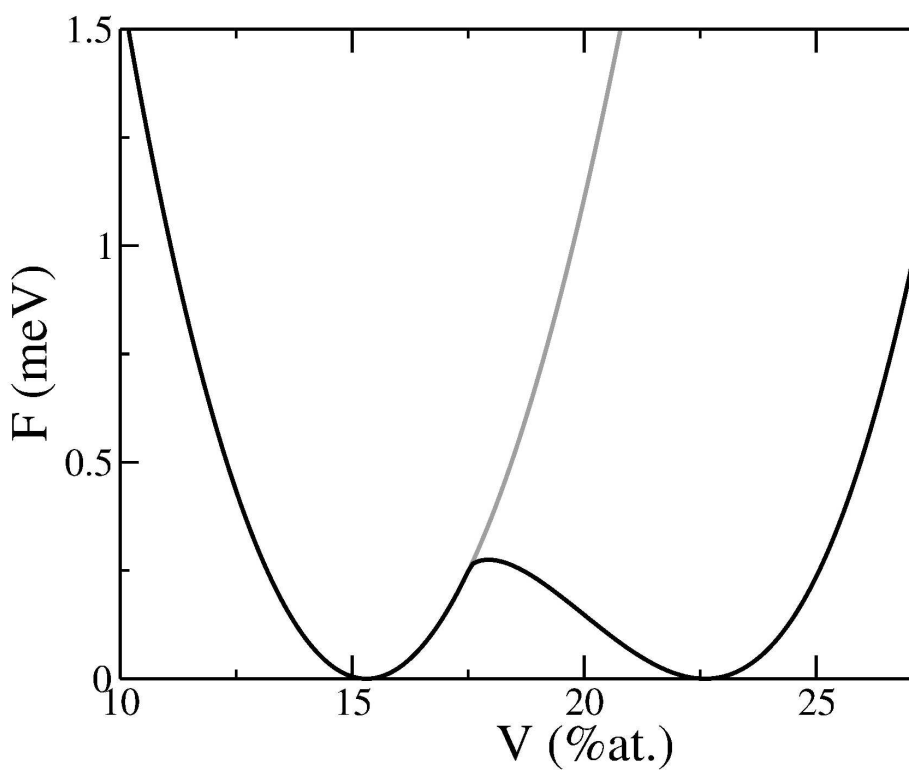


(c) variant x

257x97mm (96 x 96 DPI)

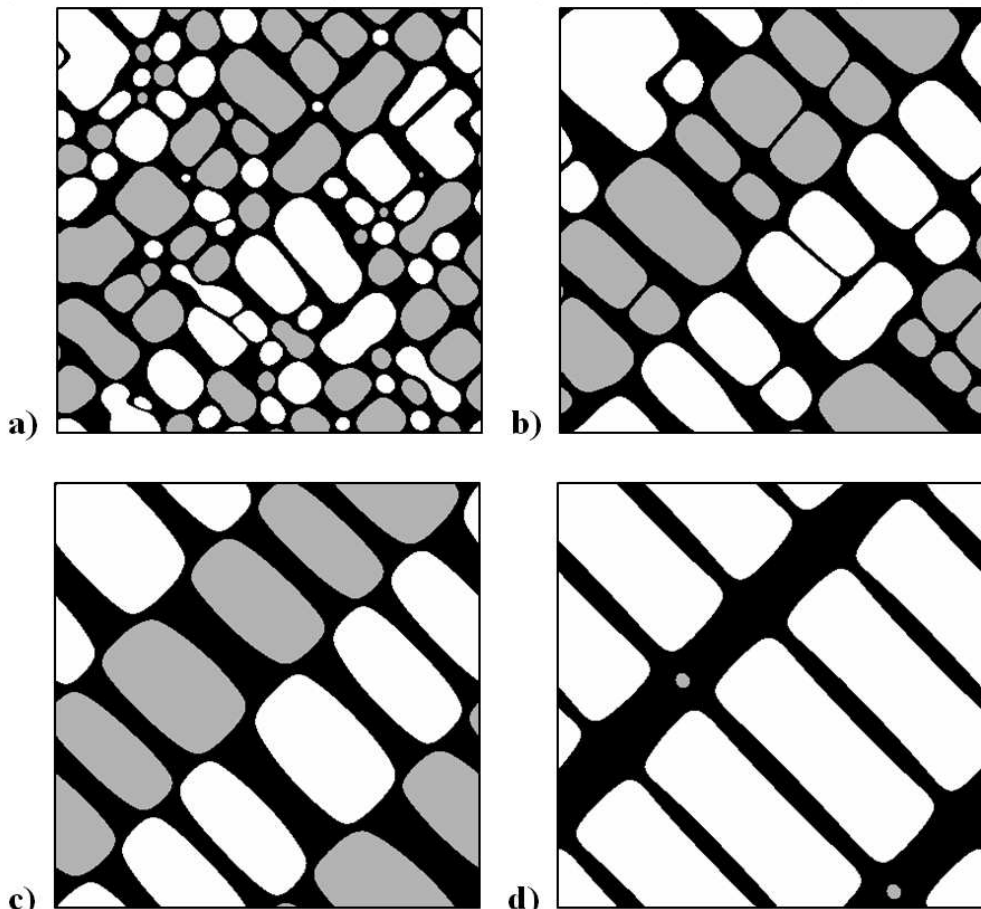
Peer Review Only

1
2
3
4
5
6
7
8
9
10
11
12
13
14
15
16
17
18
19
20
21
22
23
24
25
26
27
28
29
30
31
32
33
34
35
36
37
38
39
40
41
42
43
44
45
46
47
48
49
50
51
52
53
54
55
56
57
58
59
60



215x279mm (600 x 600 DPI)

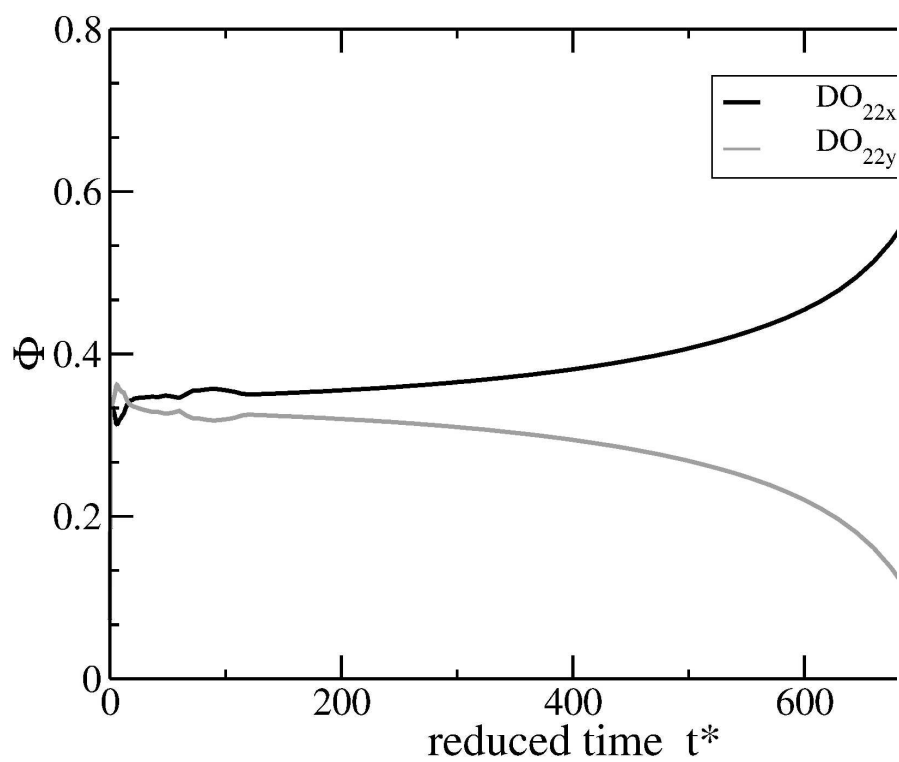
1
2
3
4
5
6
7
8
9
10
11
12
13
14
15
16
17
18
19
20
21
22
23
24
25
26
27
28
29
30
31
32
33
34
35
36
37
38
39
40
41
42
43
44
45
46
47
48
49
50
51
52
53
54
55
56
57
58
59
60



237x220mm (96 x 96 DPI)

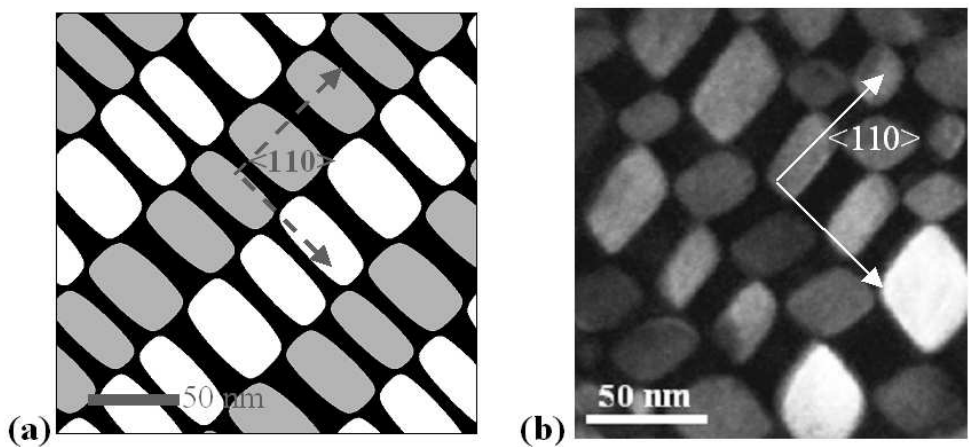
Only

1
2
3
4
5
6
7
8
9
10
11
12
13
14
15
16
17
18
19
20
21
22
23
24
25
26
27
28
29
30
31
32
33
34
35
36
37
38
39
40
41
42
43
44
45
46
47
48
49
50
51
52
53
54
55
56
57
58
59
60



215x279mm (600 x 600 DPI)

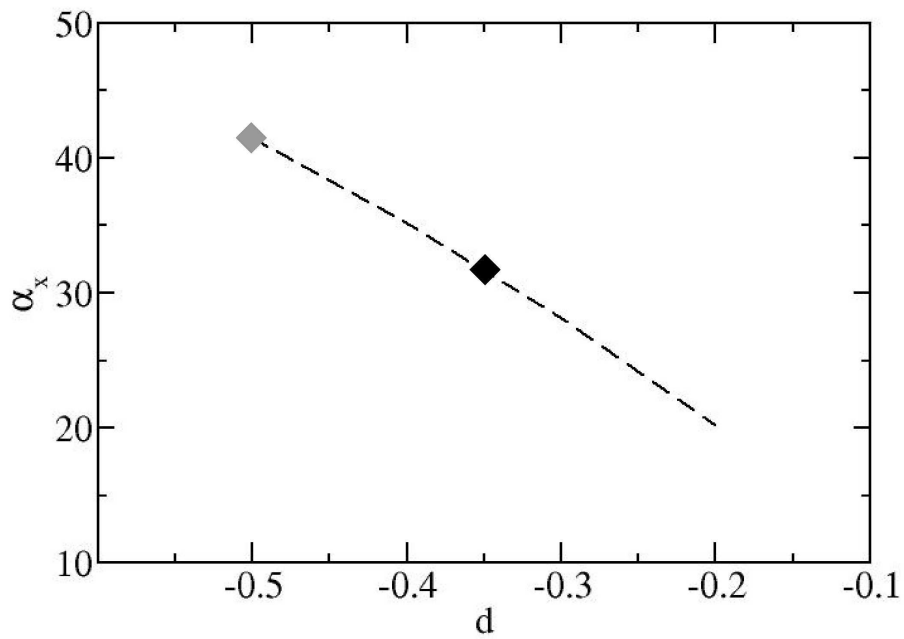
1
2
3
4
5
6
7
8
9
10
11
12
13
14
15
16
17
18
19
20
21
22
23
24
25
26
27
28
29
30
31
32
33
34
35
36
37
38
39
40
41
42
43
44
45
46
47
48
49
50
51
52
53
54
55
56
57
58
59
60



231x108mm (96 x 96 DPI)

er Review Only

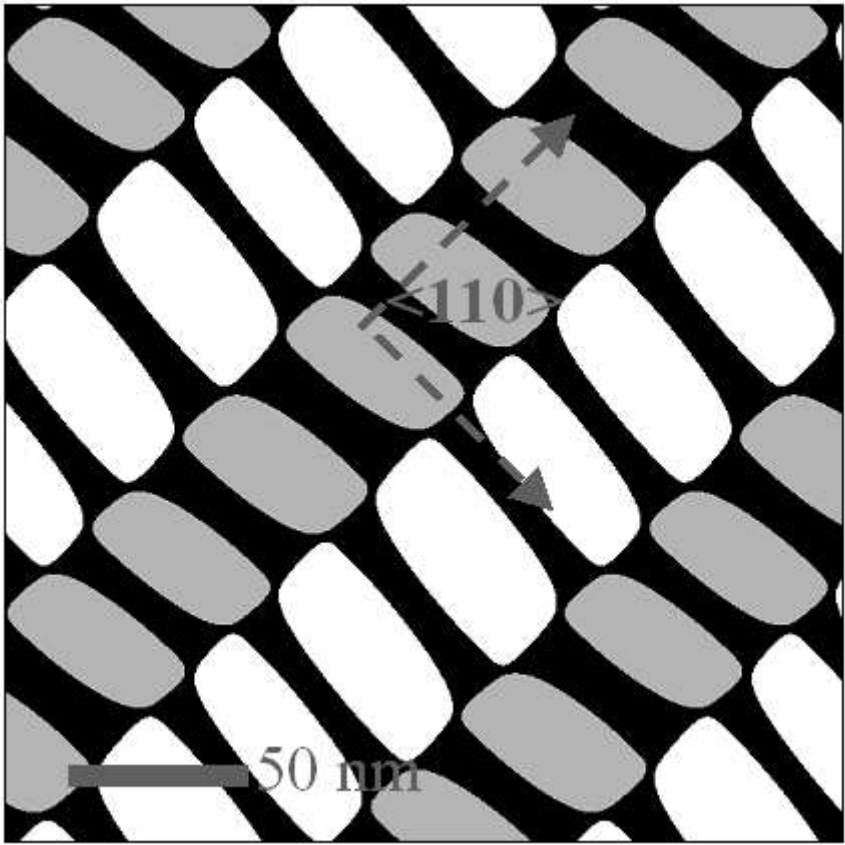
1
2
3
4
5
6
7
8
9
10
11
12
13
14
15
16
17
18
19
20
21
22
23
24
25
26
27
28
29
30
31
32
33
34
35
36
37
38
39
40
41
42
43
44
45
46
47
48
49
50
51
52
53
54
55
56
57
58
59
60



197x152mm (600 x 600 DPI)

Pre-proof Only

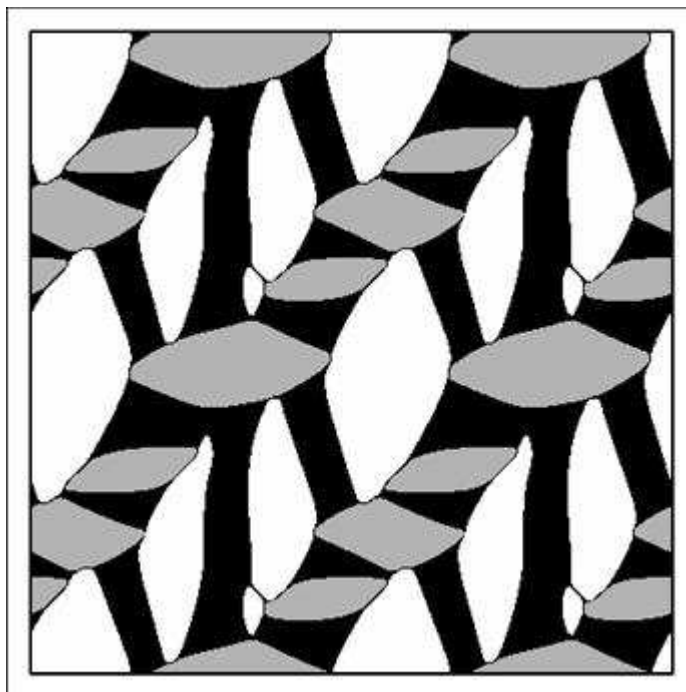
1
2
3
4
5
6
7
8
9
10
11
12
13
14
15
16
17
18
19
20
21
22
23
24
25
26
27
28
29
30
31
32
33
34
35
36
37
38
39
40
41
42
43
44
45
46
47
48
49
50
51
52
53
54
55
56
57
58
59
60



118x118mm (96 x 96 DPI)

Only

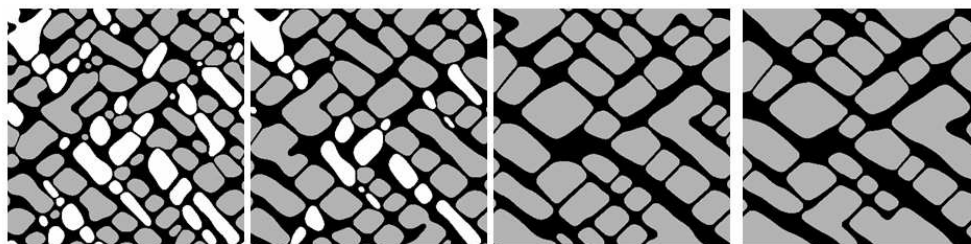
1
2
3
4
5
6
7
8
9
10
11
12
13
14
15
16
17
18
19
20
21
22
23
24
25
26
27
28
29
30
31
32
33
34
35
36
37
38
39
40
41
42
43
44
45
46
47
48
49
50
51
52
53
54
55
56
57
58
59
60



58x58mm (150 x 150 DPI)

View Only

1
2
3
4
5
6
7
8
9
10
11
12
13
14
15
16
17
18
19
20
21
22
23
24
25
26
27
28
29
30
31
32
33
34
35
36
37
38
39
40
41
42
43
44
45
46
47
48
49
50
51
52
53
54
55
56
57
58
59
60



a)

b)

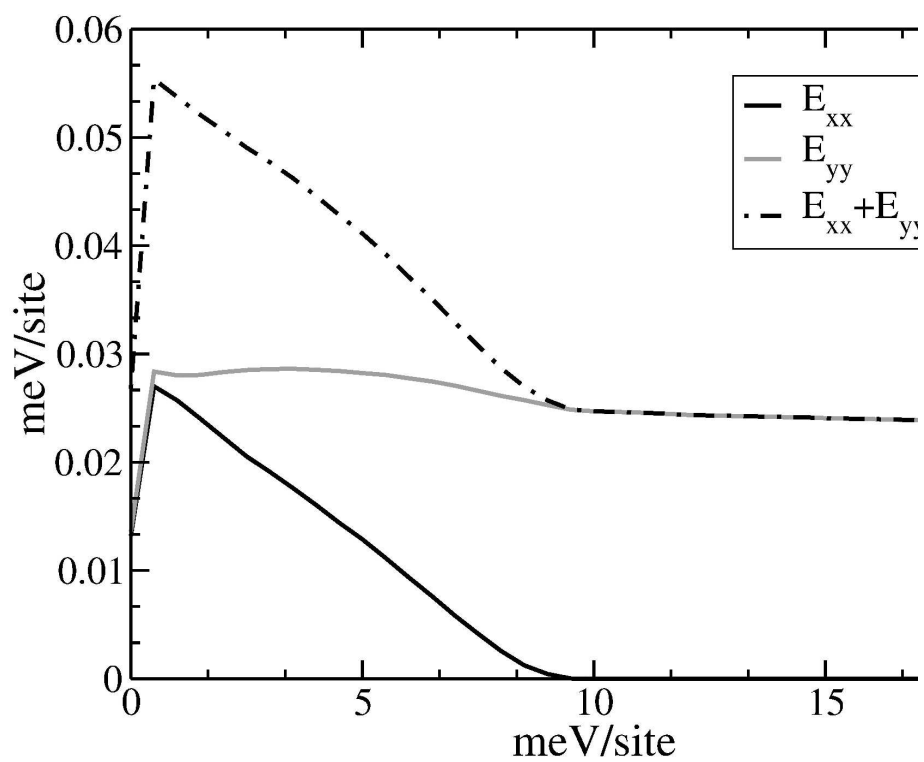
c)

d)

253x75mm (96 x 96 DPI)

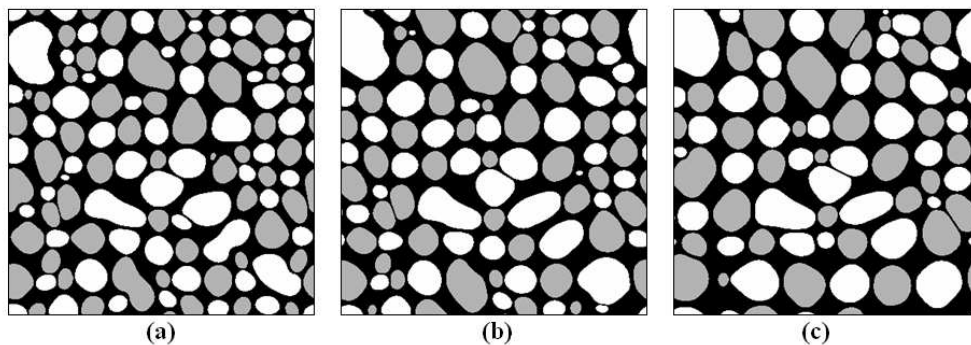
Peer Review Only

1
2
3
4
5
6
7
8
9
10
11
12
13
14
15
16
17
18
19
20
21
22
23
24
25
26
27
28
29
30
31
32
33
34
35
36
37
38
39
40
41
42
43
44
45
46
47
48
49
50
51
52
53
54
55
56
57
58
59
60



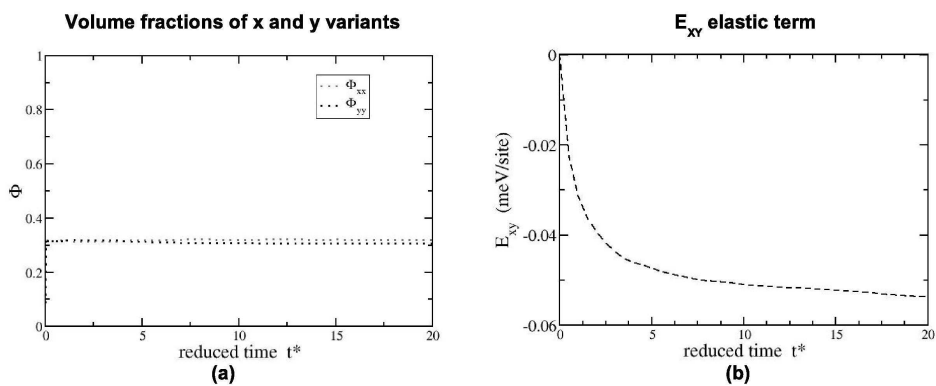
215x279mm (600 x 600 DPI)

1
2
3
4
5
6
7
8
9
10
11
12
13
14
15
16
17
18
19
20
21
22
23
24
25
26
27
28
29
30
31
32
33
34
35
36
37
38
39
40
41
42
43
44
45
46
47
48
49
50
51
52
53
54
55
56
57
58
59
60



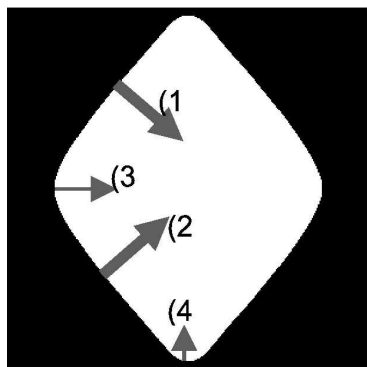
245x87mm (96 x 96 DPI)

Peer Review Only

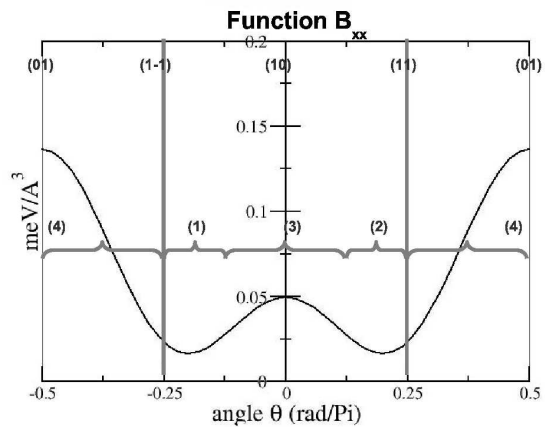


108x45mm (600 x 600 DPI)

1
2
3
4
5
6
7
8
9
10
11
12
13
14
15
16
17
18
19
20
21
22
23
24
25
26
27
28
29
30
31
32
33
34
35
36
37
38
39
40
41
42
43
44
45
46
47
48
49
50
51
52
53
54
55
56
57
58
59
60



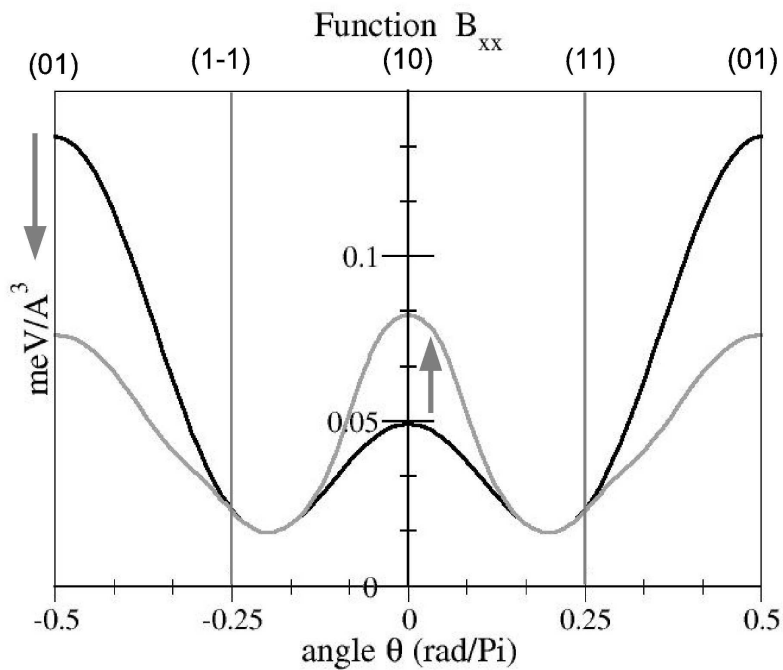
(a)



(b)

143x84mm (600 x 600 DPI)

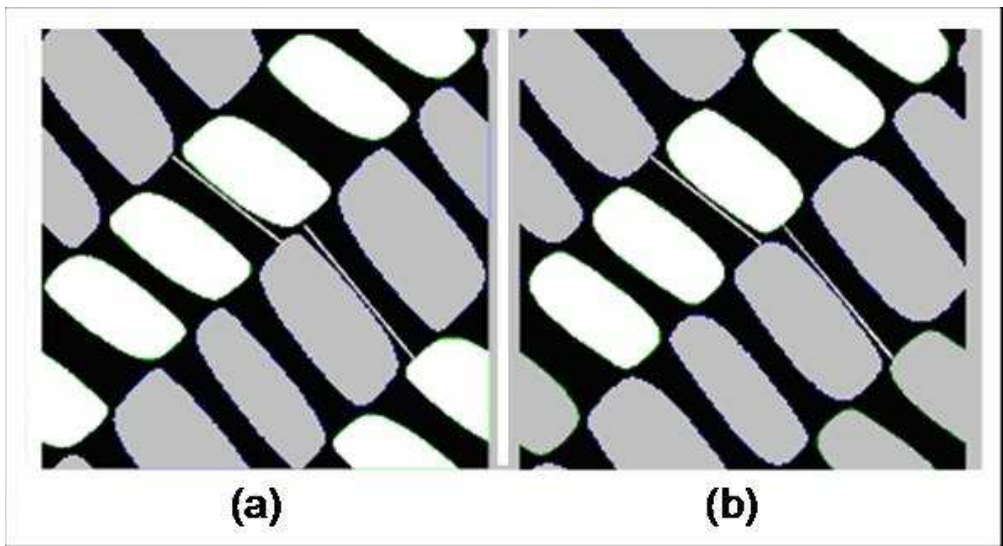
Review Only



197x139mm (600 x 600 DPI)

1
2
3
4
5
6
7
8
9
10
11
12
13
14
15
16
17
18
19
20
21
22
23
24
25
26
27
28
29
30
31
32
33
34
35
36
37
38
39
40
41
42
43
44
45
46
47
48
49
50
51
52
53
54
55
56
57
58
59
60

1
2
3
4
5
6
7
8
9
10
11
12
13
14
15
16
17
18
19
20
21
22
23
24
25
26
27
28
29
30
31
32
33
34
35
36
37
38
39
40
41
42
43
44
45
46
47
48
49
50
51
52
53
54
55
56
57
58
59
60



100x54mm (150 x 150 DPI)

Review Only